# Chiral Templating in a Hybrid Chromium Chloride Hydrate

Joseph T. Race, Cierra Foster, Patrick M. Woodward*

Department of Chemistry and Biochemistry, The Ohio State University, 100 W. 18th Avenue, Columbus, Ohio, 43210, United States

**ABSTRACT:** The synthesis and characterization of three new hybrid metal halide hydrates in which *mer*-$[Cr^{III}Cl_3(H_2O)_3]^0$ co-crystalizes alongside α-methylbenzylammonium chloride are described. The enantiomorphic crystals, ((*R*)-(+)-α-methylbenzylammonium)$_2$(*mer*-$[CrCl_3(H_2O)_3]$)$Cl_2$ ((*R*)-**1**) and ((*S*)-(–)-α-methylbenzylammonium)$_2$(*mer*-$[CrCl_3(H_2O)_3]$)$Cl_2$ ((*S*)-**1**), have $C222_1$ space group symmetry and show mirrored circular dichroism signals. The racemate, (*rac*-α-methylbenzylammonium)$_2$(*mer*-$[CrCl_3(H_2O)_3]$)$Cl_2$ ((*rac*)-**1**), adopts a polar structure with *Cm* space group symmetry in which enantiomers are related by mirror planes within organic bilayers. Alongside detailed crystallography and magnetism of each compound, the optical properties of the *mer*-$[Cr^{III}Cl_3(H_2O)_3]^0$ unit are revisited. Understanding the intermolecular forces that stabilize each of these crystal structures lends insight into crystal engineering methodologies for stabilizing non-centrosymmetric hybrid metal halides.

## Introduction

Non-centrosymmetric (NSC) crystals, those lacking inversion symmetry, are sought after in many fields for their unique properties such as second-harmonic generation[1], piezoelectricity[2], circular dichroism[3] or pyroelectricity[4] The crystal class symmetry requirements for each of these properties was discussed thoroughly by Ok et al.[5] There are 21 NCS crystal classes, 11 of which are chiral (1, 2, 3, 4, 6, 222, 422, 622, 32, 432, 23) meaning they possess a handedness, and 10 of which are polar (1, 2, 3, 4, 6, *m*, *mm*2, 4*mm*, 6*mm*, 3*m*) meaning they possess a polar axis. The compounds reported in this work have the crystal class of either 222 (NCS and chiral, but not polar) or *m* (NCS and polar, but not chiral).

Hybrid metal halides are attractive compounds for achieving the symmetries required for these NCS materials properties because of their low-temperature, solution processibility[6] as well as variability in their composition and structure.[7] There is a particular interest in incorporating enantiomerically-pure chiral molecules into metal halide structures to template chirality into the metal halide fragments and force the structure into an NCS, chiral crystal class.[8] This strategy requires the use of enantiomerically-pure chiral molecules, purification that can add cost or time to the synthetic process. The stabilization of NCS crystals with non-chiral molecules or even racemic mixtures of chiral molecules would be attractive and is an active field of crystal engineering. For more details the interested reader can find a thorough discussion of the crystal classes of achiral NCS racemates in Wang, et al.[9] A key takeaway point is that in achiral NCS racemates when enantiomers are related by mirror planes or glide planes the crystal adopts a polar structure (point group: *m*, *mm*2, 4*mm*, 6*mm*, or 3*m*).

In this work we set out to investigate the crystal symmetries of hybrid chromium(III) chlorides containing the chiral molecule (*R/S*)-α-methylbenzylammonium, which has been shown to template chirality in many different hybrid metal halide structures.[10,11] The compounds that are the subject of this study are enantiomorphic crystals, ((*R*)-(+)-α-methylbenzylammonium)$_2$(*mer*-$[Cr^{III}Cl_3(H_2O)_3]$)$Cl_2$ ((*R*)-**1**) and ((*S*)-(–)-α-methylbenzylammonium)$_2$(*mer*-$[Cr^{III}Cl_3(H_2O)_3]$)$Cl_2$ ((*S*)-**1**) as well as the racemic crystal (*rac*-α-methylbenzylammonium)$_2$(*mer*-$[Cr^{III}Cl_3(H_2O)_3]$)$Cl_2$ ((*rac*)-**1**). These compounds can be thought of as a co-crystal between *mer*-$[Cr^{III}Cl_3(H_2O)_3]^0$ and α-methylbenzylammonium chloride. (*R*)-**1**, (*S*)-**1**, and (*rac*)-**1** belong to a group of hybrid metal halide hydrates with the general formula $A_2$(*mer*-$[M^{III}X_3(H_2O)_3]$)$X_2$ or A'(*mer*-$[M^{III}X_3(H_2O)_3]$)$X_2$, where A is a protonated amine, A' is molecule with two protonated amines groups, M is a metal with a +3 oxidation state, and $X^-$ is a halide. We were unable to find structures containing molecules with a single protonated amine group, however, two compounds with the general formula A'(*mer*-$[Fe^{III}Cl_3(H_2O)_3]$)$Cl_2$ were found in the Cambridge Structural Database (April 2024).[12,13]

This work discusses in detail the covalent bonding in the *mer*-$[CrCl_3(H_2O)_3]^0$ complexes and the non-covalent interactions (dispersion forces and hydrogen bonding) that stabilize the structures through single crystal X-ray diffraction studies. We studied the optical and magnetic properties of each compound as well as their thermal stability. Our discussion on the packing of chiral molecules containing aromatic rings aims to provide a crystal engineering strategy for the stabilization of polar, achiral racemates.

## Experimental Section

The following reagents were purchased and used as received: (*R*)-(+)-α-methylbenzylamine (ChiPros®, produced by BASF, ≥99.0%), (*S*)-(–)-α-methylbenzylamine (ChiPros®, produced by BASF, ≥99.0%), $CrCl_3 \cdot 6\ H_2O$ (Aldrich, purum p.a., ≥98% (RT)), and HCl (Fisher Scientific, 37%, *aq*).

Single crystals of (*R*)-**1**, (*S*)-**1**, and (*rac*)-**1** were similarly grown by the solvent evaporation method in a corrosion resistant chemical hood. For example, take the synthesis of (*R*)-**1**. First, $CrCl_3 \cdot 6\ H_2O$ (1.58 mmol, 421.9 mg) and 4.0 mL of 12.1 M HCl (*aq.*) were added to a 20 mL glass vial. Next, (*R*)-(+)-α-methylbenzylamine (3.17 mmol, 0.403 mL) was slowly added to the above solution, generating white smoke in the neutralization process. The solution was stirred on a hot plate at 100 °C until all solids were dissolved then the stir bar was removed. The solution in the vial was then left on the hot plate at 100 °C without a lid for approximately 10 h to concentrate the solution and initiate crystallization. Small green block crystals were isolated from the mother liquor for single-crystal X-ray diffraction studies. The remaining crystals were put in a drying oven at 80 °C for 0.5 h to remove excess solvent then using an agate mortar and pestle were ground into a light green powder for bulk sample analysis. Yields for all three compounds were quantitative. *Caution*: Volatilization of concentrated hydrochloric acid solutions can be dangerous; exposure may cause severe skin burns, eye damage, and respiratory irritation. Be sure to implement engineering controls (performing in a chemical hood), wear proper PPE, and minimize the amount of acid volatized. Full synthetic details for all three compounds can be found in the Supporting Information.

Single-crystal X-ray diffraction (SCXRD) studies were conducted on a Bruker D8 Venture Diffractometer-Mo-TXS equipped with a Bruker PHOTON III detector and a molybdenum rotating anode source (λ = 0.71073 Å) operating at 50 kV and 50 mA. Crystal temperatures during data collection were controlled using an Oxford Cryosystems Cryostream. Data were integrated using the SAINT software program[14] and scaled using the SADABS software program.[15] Crystal structures were solved by intrinsic

phasing using SHELXT.[16] Non-hydrogen atoms were first refined isotropically followed by anisotropic refinement by full matrix least-squares calculations based on $R^2$ using ShelXL.[17] Hydrogen atoms were first located in the difference map then positioned geometrically and allowed to ride on their respective parent atoms.

Powder X-ray diffraction (PXRD) data were collected using a Bruker D8 Advance diffractometer (40 kV, 40 mA; sealed Cu X-ray tube) equipped with a Johansson-type quartz monochromator and a Lynx Eye XE-T position-sensitive detector. PXRD refinements were performed using the Topas-Academic (ver. 6) software package.[18] Crystal structures were visualized with the VESTA (ver. 3) software program.[19]

UV-visible diffuse reflectance spectroscopy (DRS) data were collected from 250–850 nm with a PerkinElmer Lambda 950 spectrometer equipped with a 60 mm InGaAs integration sphere. The spectrometer was calibrated by using a Labsphere Certified Reflectance Standard. DRS data were converted to absorbance using the Kubelka-Munk transform. Absorbance peaks were fit in OriginPro 9 (Academic) using three Gaussian peaks.[20] Photoluminescence emission data were collected on powders with a Horiba Fluorolog-3 (Xenon source, 2 nm excitation and emission slit widths, 0.125 nm step size, 0.2 s integration time) equipped with a solids sample holder. Circular dichroism (CD) measurements of powdered samples were collected from 250-850 nm with a Jasco J-815 CD spectrometer in the reflection geometry. DC magnetic susceptibility measurements were measured using a Quantum Design Magnetic Property Measurement System (MPMS) SQUID magnetometer. Powdered samples of approximately 55 mg were encapsulated in gel capsules, which were inserted into the center of a plastic straw and then mounted in the magnetometer. Data were collected between 2 K and 300 K under both zero-field-cooled (ZFC) and field-cooled (FC) conditions with an applied field of 1000 Oe. Thermal gravimetric analysis (TGA) measurements were performed on a TA Instruments TGA 550 in platinum pans. Samples were heated from ambient temperature to 690 K at a rate of 10 K/min under a nitrogen stream of 25 mL/min.

**Results and Discussion**

**Structure.** The crystal structures of (*R*)-**1**, (*S*)-**1**, and (*rac*)-**1** were determined at 100 K through SCXRD studies. Full details of the SCXRD studies can be found in the Supporting Information (Table S1). PXRD studies of powders of each compound at room temperature reveal they maintain their 100 K crystal structures up to room temperature and are phase pure (Figure S1).

The enantiomorphs, (*R*)-**1** and (*S*)-**1,** both have $C222_1$ (#20) space group symmetry with similar sized unit cells of ~2400 Å$^3$ (Table 1). $C222_1$ (#20) is a non-centrosymmetric space group which is chiral and non-polar. Each enantiomorph can be thought of as a co-crystal between *mer*-$[CrCl_3(H_2O)_3]^0$ and the corresponding enantiomer of α-methylbenzylammonium (α-MBzA) chloride. The crystal structures of (*R*)-**1** and (*S*)-**1** are nearly identical except for their handedness and therefore for simplicity only the structure of (*R*)-**1** will be discussed here. The crystal structure of (*S*)-**1** is depicted in the Supporting Information (Figure S2).

**Table 1**. Crystal structure summaries of ((*R*)-(+)-α-MBzA)$_2$(*mer*-$[CrCl_3(H_2O)_3]$)$Cl_2$ ((*R*)-**1**), ((*S*)-(–)-α-MBzA)$_2$(*mer*-$[CrCl_3(H_2O)_3]$)$Cl_2$ ((*S*)-**1**), and (*rac*-α-MBzA)$_2$(*mer*-$[CrCl_3(H_2O)_3]$)$Cl_2$ ((*rac*)-**1**).

| Empirical formula | $C_{16}H_{30}Cl_5CrN_2O_3$ | | |
|---|---|---|---|
| Formula weight (g/mol) | 527.67 | | |
| Temperature (K) | 100 | 100 | 100 |
| Crystal system | Orthorhombic | Orthorhombic | Monoclinic |
| Space group | $C222_1$ | $C222_1$ | $Cm$ |
| a (Å) | 7.3695(4) | 7.3666(4) | 7.3599(3) |
| b (Å) | 10.4283(4) | 10.4278(5) | 31.024(1) |
| c (Å) | 31.233(1) | 31.225(1) | 6.2449(2) |
| α (°) | 90 | 90 | 90 |
| β (°) | 90 | 90 | 123.322(1) |
| γ (°) | 90 | 90 | 90 |
| V (Å$^3$) | 2400.3(2) | 2398.7(2) | 1191.51(8) |
| Z | 4 | 4 | 2 |
| Cr–Cl (trans to Cl) bond length (Å) | 2.3105(7) | 2.3093(7) | 2.3060(7) |
| | 2.3105(7) | 2.3093(7) | 2.3060(7) |
| Cr–Cl (trans to $H_2O$) bond length (Å) | 2.3035(7) | 2.3045(9) | 2.3099(9) |
| Cr–O (trans to $H_2O$) bond length (Å) | 1.988(1) | 1.989(1) | 1.979(4) |
| | 1.988(1) | 1.989(1) | 1.998(4) |
| Cr–O (trans to Cl) bond length (Å) | 1.999(1) | 2.001(3) | 2.003(3) |

First we focus on the isolated *mer*-$[CrCl_3(H_2O)_3]^0$ pseudo-octahedra which pack into layers separated by bilayers of organic molecules (Figure 1). Cr–ligand bond distances for ligands trans to the same ligand type (i.e., $Cl^-$ trans to $Cl^-$) are 1.988(1) Å for Cr–O bonds and 2.3105(7) Å for Cr–Cl bonds, consistent with prior studies.[21,22] The $H_2O$ and $Cl^-$ ligands trans to one another have Cr–ligand bond lengths of 1.999(1) Å and 2.3035(7) Å, respectively. The subtle shortening of the Cr–Cl bond and the lengthening of the Cr–O bond can be explained by the trans influence effect. Ligands trans to one another use the same orbitals on the metal for bonding, for σ-bonding interactions with Cr those would be the $3dz^2$ and $3dx^2–y^2$ orbitals. $Cl^-$ is a stronger σ-donor than $H_2O$, meaning the O of the $H_2O$ ligand cannot donate electrons to the metal as well. This weakens the σ-bonding interaction between Cr and $H_2O$, leading to a longer Cr–O bond length. Within a given layer, *mer*-$[CrCl_3(H_2O)_3]^0$ pseudo-octahedra pack in a parallel direction with their dipoles along the [010] direction, however, in the adjacent layer the pseudo-octahedra pack in the exact opposite direction, with dipoles along $[0\bar{1}0]$, canceling any net dipole moment.

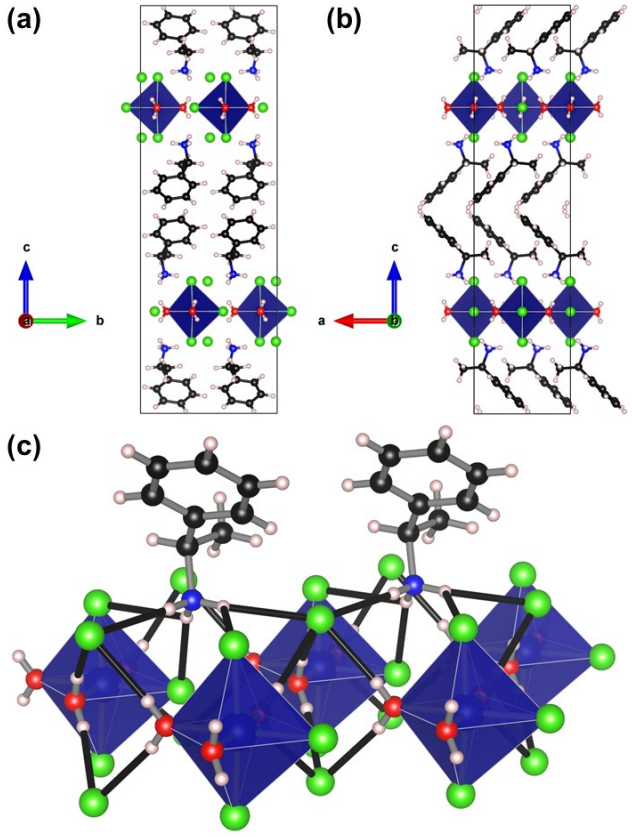


**Figure 1.** Crystal structure of (*R*)-**1** at 100 K along (a) the *a*-axis and (b) the *b*-axis. (c) Hydrogen bonding network in (*R*)-**1**. Cr-centered pseudo-octahedra are blue. Chlorine, oxygen, nitrogen, carbon, and hydrogen are represented by green, red, blue, black, and white spheres, respectively. Thick black lines denote hydrogen bonds.

Sitting above and below the void in each *mer*-$[CrCl_3(H_2O)_3]^0$ layer are isolated $Cl^-$ anions which function as hydrogen bond acceptors with the three water molecules coordinating chromium (Figure 1c). O–H…$Cl^-$ hydrogen bond distances and angles range from 2.29(4) Å to 2.34(4) Å and from 158(4)° to 169(4)°, respectively. Not only do these free $Cl^-$ anions help with charge balance, but they also help stabilize the *mer*-$[CrCl_3(H_2O)_3]^0$ isomer by stabilizing the water ligands in the equatorial plane through hydrogen bonding interactions.

Finally, the last component of the enantiomorphic structures is the α-methylbenzylammonium molecule. Like the isolated $Cl^-$ anions, the (*R*)-α-$MBzA^+$ molecules sit above and below the voids in the *mer*-$[CrCl_3(H_2O)_3]^0$ layers, and are symmetry related to one another by 2-fold rotation axes and $2_1$ screw axes. (*R*)-α-$MBzA^+$ molecules form organic bilayers between *mer*-$[CrCl_3(H_2O)_3]^0$ layers, packing with a herring-bone pattern stabilized by CH–π edge-to-face interactions between aromatic rings across the bilayer (Figure 1b). The strength of the CH–π edge-to-face interaction is dictated by 1) the C–H…phenyl ring centroid distance and 2) the C–H…phenyl ring centroid angle. Shorter distances and angles closer to 180° are indicative of stronger interactions. In (*R*)-**1**, C–H…phenyl ring centroid distances and angles are 2.918 Å and 142.22°, respectively. C–H…phenyl ring centroid distances and angles for each structure can be found in Table S2.

The $–NH_3^+$ groups of the (*R*)-α-$MBzA^+$ molecules are anchored to the *mer*-$[CrCl_3(H_2O)_3]^0$ layers with hydrogen bonds. Each (*R*)-α-$MBzA^+$ molecule acts as a hydrogen bond donor and forms three hydrogen bonding interactions (Figure 1c). The first interaction is a hydrogen bond with an isolated $Cl^-$ anion (2.4127(6) Å and 160.7(1)°). The second interaction is a bifurcated hydrogen bond between an equatorial $Cl^-$ anion (2.3360(1) Å and 150.3(1)°) and an axial $Cl^-$ anion (2.8659(5) Å and 119.7(1)°) coordinated to a single chromium. The third interaction is another bifurcated hydrogen bond between an isolated $Cl^-$ anion (2.6611(5) Å and 152.4(1)°) and an axial $Cl^-$ anion (2.7955(7) Å and 117.5(1)°) coordinated to chromium. Hydrogen bond distances, donor-acceptor distances, and hydrogen bond angles in each structure can be found in Tables S3-S5.

The racemic crystal, (*rac*)-**1**, has *Cm* (#8) space group symmetry with a unit cell volume (V = 1191.51(8) $Å^3$) roughly half that of the enantiomorphic crystals (*R*)-**1** and (*S*)-**1** (V = ~2400 $Å^3$) and unit cell dimensions of a = 7.3599(3) Å, b = 31.024(1) Å, c = 6.2449(2) Å, and β = 123.322(1)°. The structural components of the racemate are similar to the enantiomorphs; isolated *mer*-$[CrCl_3(H_2O)_3]^0$ pseudo-octahedra layers, isolated $Cl^-$ anions, and α-$MBzA^+$ molecules (Figure 2). However, there are crucial differences that stabilize this structure in the space group *Cm* (#8); a non-centrosymmetric, achiral, polar space group.

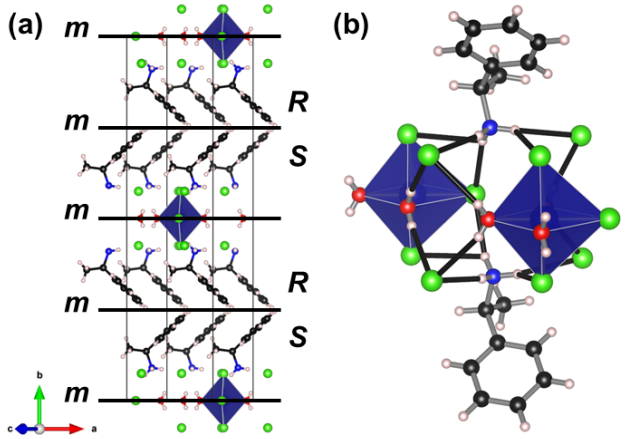


**Figure 2.** (a) Crystal structure of (*rac*)-**1** at 100 K along the *c**-axis. (b) Hydrogen bonding network in (*rac*)-**1**. Cr-centered pseudo-octahedra are blue. Chlorine, oxygen, nitrogen, carbon, and hydrogen are represented by green, red, blue, black, and white spheres, respectively. Thick black lines in (a) represent mirror planes (*m*). *R* and *S* labels represent layers of (*R*)-(+)-α-methylbenzylammonium molecules and (*S*)-(–)-α-methylbenzylammonium molecules, respectively. Thick black lines in (b) denote hydrogen bonds.

The driving force for the stabilization of this polar structure appears to be the packing of (*R*)-α-$MBzA^+$ and (*S*)-α-$MBzA^+$ molecules in the structure. The α-substituted methyl group of each enantiomer makes it sterically unfavorable for both enantiomers to pack into the same side of the organic bilayer. Therefore, each enantiomer packs into its own half of the organic bilayer resulting in parallel alignment of molecular dipole moments along the [100] direction and a bisecting mirror plane relating the enantiomers by symmetry (Figure 2a). This creation of enantiomerically pure organic layers templates the packing of *mer*-$[CrCl_3(H_2O)_3]^0$ units to orient in a parallel fashion from one *mer*-$[CrCl_3(H_2O)_3]^0$ layer to the next, with *mer*-$[CrCl_3(H_2O)_3]^0$ dipole moments pointing in the [001] direction. The separation of α-$MBzA^+$ enantiomers into

separate layers does not disrupt the CH–π edge-to-face interactions across the organic bilayer, instead, the interaction appears to be slightly stronger in the racemate as compared to the enantiomorphs (Table S2). Stronger phenyl ring interactions could be a contributing factor to the slightly higher density of (*rac*)-**1** (1.471 g/cm$^3$ at 100 K) compared to (*R*)-**1** (1.460 g/cm$^3$ at 100 K) and (*S*)-**1** (1.461 g/cm$^3$ at 100 K).

The hydrogen bonding motifs in (*rac*)-**1** remain the same as in (*R*)-**1** and (*S*)-**1**, however, the strengths of some hydrogen bonds change. Hydrogen bonds made between water molecules coordinated to chromium and isolated $Cl^-$ anions are elongated (average in (*R*)-**1** of 2.32 Å; average in (*rac*)-**1** of 2.40 Å), while hydrogen bonds between α-MBzA$^+$ molecules and isolated $Cl^-$ anions are shortened (average in (*R*)-**1** of 2.54 Å; average in (*rac*)-**1** of 2.47 Å). Hydrogen bonds made between α-MBzA$^+$ molecules and $Cl^-$ anions coordinated to chromium are elongated, much more so for those made to axial $Cl^-$ anions (average in (*R*)-**1** of 2.83 Å; average in (*rac*)-**1** of 2.93 Å).

The *mer*-$[CrCl_3(H_2O)_3]^0$ pseudo-octahedra in (*rac*)-**1** still have elongated Cr–O bonds for water molecules trans to $Cl^-$ anions, however, the corresponding shortening of Cr–Cl bonds for $Cl^-$ anions trans to water molecules isn't observed. This difference in trans influence between (*rac*)-**1** and the enantiomorphs likely arises to subtleties in the hydrogen bonding, which also influences metal–ligand bond distances in these compounds.

**Optical Properties.** $Cr^{3+}$ is in a 6-coordinate, pseudo-octahedral ligand environment in all three compounds, reported with $Cr^{3+}$ site symmetries in (*R*)-**1**, (*S*)-**1**, and (*rac*)-**1** of 2, 2 , and *m*, respectively. Using a Tanabe-Sugano diagram for a d$^3$ transition metal in an octahedral crystal field, the crystal field splitting ($\Delta_{oct}$) and Racah parameter *B* (an approximation for the strength of the bond between the metal and the ligand) can be estimated. For a d$^3$ transition metal in an octahedral crystal field there are three allowed d-to-d transitions, from lowest to highest energy they are: $^4A_{2g} \rightarrow {}^4T_{2g}$, $^4A_{2g} \rightarrow {}^4T_{1g}(F)$, and $^4A_{2g} \rightarrow {}^4T_{1g}(P)$.

Absorbance data of (*R*)-**1** and (*S*)-**1** are nearly identical showing two broad, lower intensity peaks centered at ~670 nm and ~470 nm as well as a high intensity peak centered at ~260 nm (Figure 3a). The peaks centered at ~670 nm and ~470 nm are assigned to the $^4A_{2g} \rightarrow {}^4T_{2g}$ and $^4A_{2g} \rightarrow {}^4T_{1g}(F)$ d-to-d transitions of $Cr^{3+}$. The peak centered at 670 nm has a shoulder at ~700 nm that we attribute to lower energy d-to-d transitions, resulting from splitting of the $t_{2g}$ and $e_g$ orbitals of $Cr^{3+}$ in low symmetry ligand fields. Similar splitting of the $^4A_{2g} \rightarrow {}^4T_{2g}$ band is seen in solution phase absorbance measurements of low symmetry $[CrCl_3(H_2O)_3]^0$ (*aq.*), whereas it is absent in spectra of octahedral $[Cr(H_2O)_6]^{3+}$ (*aq.*).[23] These two lowest energy peaks span most of the visible spectrum except the green region (~550 nm), the lowest energy of the two extending into the near-IR with negligible absorbance by 850 nm. The high intensity peak centered at ~260 nm coincides with the absorbance of α-MBzA which has an absorbance maxima at ~260 nm arising from π-to-π* transitions within the aromatic ring.[24] The high intensity of this peak relative to the d-to-d transitions is consistent with the high molar absorption coefficients of π-to-π* transitions.[25] Using $\Delta_{oct}$ = 1.83 eV and Racah parameter B = 0.080 eV values calculated from the two lower energy transitions, the highest energy d-to-d transition ($^4A_{2g} \rightarrow {}^4T_{1g}(P)$) is calculated to occur at ~300 nm (Table 2). Consequently, this transition is obscured by overlap with the peak from π-to-π* transitions within the α-MBzA molecules. The absorbance data of (*rac*)-**1** closely resembles that of the enantiomorphic crystals apart from higher relative intensities of the two lower energy peaks and a small red-shift in the higher energy peak (Figure 3a).

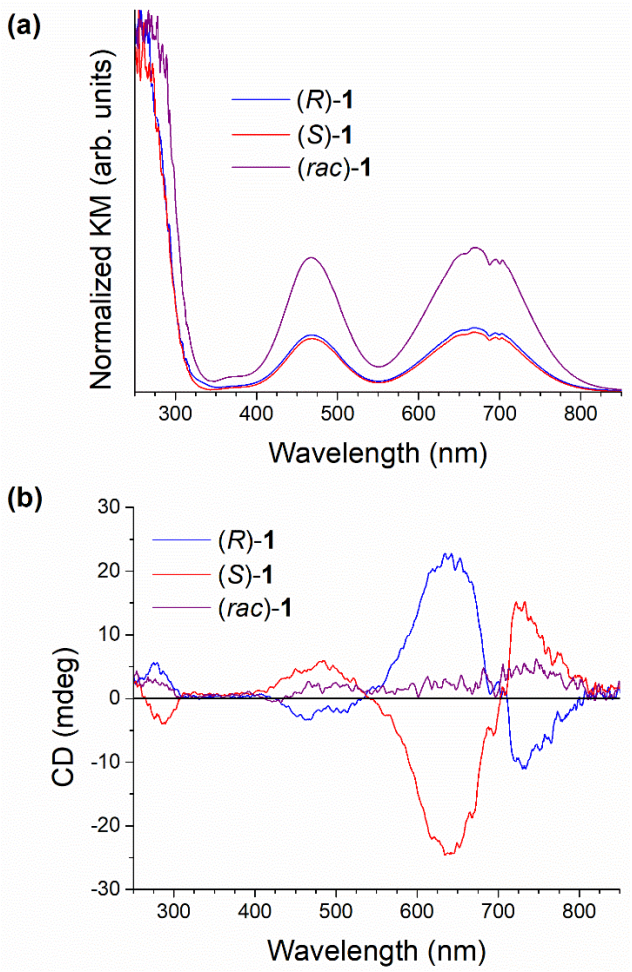


**Figure 3.** (a) Absorbance and (b) circular dichroism data for (*R*)-**1**, (*S*)-**1**, and (*rac*)-**1**.

The energies of the $A_{2g} \rightarrow {}^4T_{2g}$ and $^4A_{2g} \rightarrow {}^4T_{1g}(F)$ transitions are consistent with previously reported spectra for $[CrCl_3(H_2O)_3]^0$ in solution as well as bathochromic shifts in the absorbance bands from chromium(III) complexes with fewer coordinating $Cl^-$ ligands (Table S6 and Figure S3).

**Table 2.** Absorbance peaks in the DRS data. The position of the $^4A_{2g} \rightarrow {}^4T_{1g}(P)$ transition is calculated to be ~300 nm from the values of $\Delta_{oct}$ = 1.83 eV and B = 0.080 eV.

| Compound (Adjusted $R^2$ of Fit) | $^4A_{2g} \rightarrow {}^4T_{2g}$ | $^4A_{2g} \rightarrow {}^4T_{1g}(F)$ | $\pi \rightarrow \pi^*$ |
|---|---|---|---|
| (*R*)-**1** (0.99726) | 671 nm | 469 nm | 258 nm |
| (*S*)-**1** (0.99625) | 671 nm | 470 nm | 260 nm |
| (*rac*)-**1** (0.99179) | 672 nm | 469 nm | 267 nm |

Given their crystal classes (222 for the enantiomorphs and *m* for the racemate), all three compounds should be optically active and display circular dichroism (CD). CD spectra were collected on powdered samples in the reflection geometry over the same spectra range as the DRS data (Figure 3b). (*R*)-**1** and (*S*)-**1** have clear CD signals which mirror each other closely. At the absorbance peak centered at 671 nm, (*S*)-**1** displays a positive Cotton effect and (*R*)-**1** a negative Cotton effect. Curiously, neither enantiomorph demonstrate any Cotton effect at the absorption bands centered at 470 nm or 260 nm. (*rac*)-**1** doesn't show much CD signal despite belonging to the optically-active crystal class, *m*. We can rationalize this weakened CD signal by the fact that in the crystal class *m*, optical activity is equal and opposite in two perpendicular directions of each crystallite and because of the close to random orientation of crystallites in a powder, optical activity is diminished.[26]

Room temperature photoluminescence emission data were collected on (*R*)-**1** from 700 nm to 1000 nm using an excitation wavelength of 671 nm (Figure S4). There is no indication of emission above the background, which isn't terribly surprising given the fact that aqua ligands are known to be capable of quenching $Cr^{3+}$ luminescence.[27] While $Cr^{3+}$ is a well-known luminescent ion in stiff lattices like ruby ($Al_2O_3$:$Cr^{3+}$), when coordinated by aqua ligands high frequency O–H vibrations increase the rate of non-radiative relaxation from excited states.[28] We hypothesize that the aqua ligands coordinated to $Cr^{3+}$ quench any potential room temperature photoluminescence in these compounds, however, photoluminescence may well emerge at low temperature where the thermal population of high frequency O–H vibrations is diminished.

**Magnetism**. Temperature-dependent magnetic susceptibility measurements were collected on (*R*)-**1**, (*S*)-**1**, and (*rac*)-**1** from 300 K to 2 K and under a magnetic field of 1 kOe. All three compounds exhibited Curie paramagnetic behavior down to 2 K. $\chi^{-1}$ v. T plots were fit using the Curie-Weiss law (Curie and Weiss constants in Table S7) and $\mu_{eff}$ were determined to be 3.81 $\mu_B$, 3.82 $\mu_B$, and 3.82 $\mu_B$ for (*R*)-**1**, (*S*)-**1**, and (*rac*)-**1**, respectively. These $\mu_{eff}$ values align well with the calculated spin-only $\mu_{eff}$(calc.) of 3.87 $\mu_B$ for a $d^3$ $Cr^{3+}$ ion. The Wiess constants range from −0.09 K to +0.16 K, from which we can conclude that coupling between neighboring $Cr^{3+}$ ions is negligible. We attribute this behavior to the large separations between $Cr^{3+}$ magnetic centers and the lack of covalent bonding between $[CrCl_3(H_2O)_3]$ complexes. The shortest intra-layer Cr–Cr distance in (*R*)-**1** is 6.3847(3) Å, which rules out direct exchange interactions between 3d orbitals of adjacent $Cr^{3+}$ centers. The fact that no ligand binds to more than one $Cr^{3+}$ center helps to explain why superexchange interactions are also exceedingly weak.

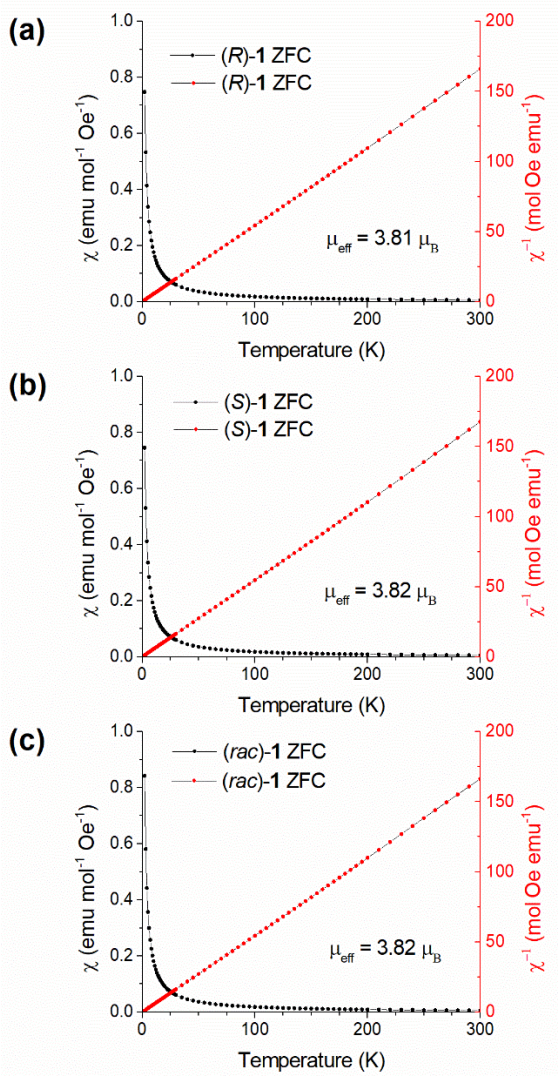


**Figure 4.** Magnetic susceptibility and inverse susceptibility for (a) (*R*)-**1**, (b) (*S*)-**1**, and (c) (*rac*)-**1**. In all compounds, the zero-field-cooled and field-cooled data lie directly on top of each other (Figure S5).

**Thermal Stability.** Thermogravimetric analysis (TGA) data were collected on powdered samples of (*R*)-**1**, (*S*)-**1**, and (*rac*)-**1** (Figure 5). TGA data for all three samples are nearly identical, unsurprising given their compositional similarities, therefore for brevity, only TGA data of (*R*)-**1** will be discussed. (*R*)-**1** is ideally comprised of 10.25 weight % $H_2O$, 59.75 weight % (*R*)-(+)-α-MBzACl, and 30 weight % $CrCl_3$. Decomposition appears to happen in roughly two steps: loss of water from the structure and volatilization of the organic. The loss of water from the structure starts at 389 K and ends at 451 K, representing a loss of 11.26 weight %. The volatilization of (*R*)-(+)-α-MBzACl starts slowly at 487 K, increases rapidly at 547 K, slows down at 603 K, and ends at 681 K, representing a loss of 61.68 weight %. The residual of 27.06 weight % suggests only anhydrous $CrCl_3$ remains, which is likely given that $CrCl_3$ isn't reported to volatilize until 776 K.[29] In order to definitively identify the species volatilizing and the phases remaining after each decomposition step, more qualitative measurements like mass spectroscopy or PXRD are required.

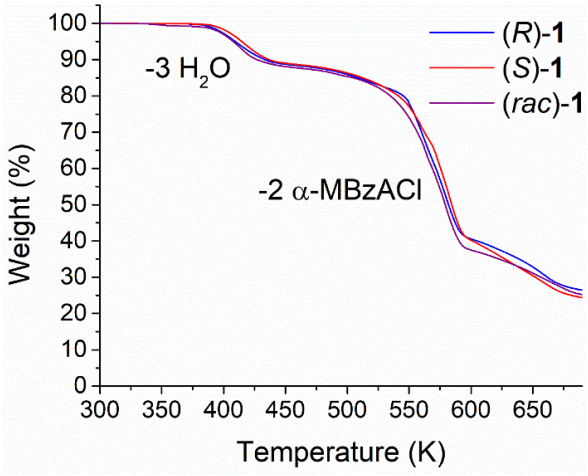


**Figure 5.** Thermogravimetric analysis (TGA) data of (*R*)-**1**, (*S*)-**1**, and (*rac*)-**1** powders.

TGA data collected on (*R*)-**1** indicates that dehydration starts at 390 K and ends at 450 K, however, that data doesn't lend any insight into what might be going on structurally. To evaluate this, light green (*R*)-**1** powder was placed in an alumina crucible which was then heated in a box furnace at 383 K for 2 h to dehydrate the sample. After 2 h at 383 K, the sample was quenched to room temperature to minimize any rehydration. After dehydration, the powder had turned a violet color which, with the absence of water, suggests the formation of $CrCl_3$ which is violet in color.[30] Within 5 min of removing the sample from the box furnace, the powder was packed into a PXRD sample holder and covered with a piece of Kapton tape to prevent rehydration. PXRD data of the dehydrated sample featured a broad peak centered at 6.28° 2θ and the amorphous feature of the Kapton tape, however, no other Bragg reflections were observed (Figure S6). The lack of crystallinity in the sample makes it difficult to say if the sample has segregated into $CrCl_3$ and MBzACl or is a homogeneous but amorphous phase.

### Conclusions

Three new NCS hybrid metal halides, one of which is a polar, achiral racemate, have been synthesized and characterized. Similar to the stabilization of other $[CrCl_n(H_2O)_{6-n}]^{3-n}$ coordination isomers in the solid state, hydrogen bonding plays a vital role in stabilizing *mer*-$[CrCl_3(H_2O)_3]^0$ in these compounds. We were able to substantiate the absorbance data of $[CrCl_3(H_2O)_3]^0$ in solution[22,23] with solid state measurements of the *mer*-$[CrCl_3(H_2O)_3]^0$ isomer, using a $d^3$ octahedral Tanabe-Sugano diagram to calculate $\Delta_{oct}$ = 1.84 eV and B = 0.080 eV. Cr–Cr distances in these compounds are too large to see any exchange interactions for cooperative magnetism and all three compounds are paramagnetic down to 2 K and have exceedingly small Weiss constants. After dehydration by heating, the compounds change color to violet, indicating the possible formation of amorphous $CrCl_3$.

This result demonstrates a crystal engineering strategy to stabilize non-centrosymmetric crystal structures from racemic mixtures of chiral molecules or molecular ions. When it is energetically favorable to for chiral molecules to pack into bilayers (i.e., chiral aromatic amines), achiral racemic crystals can form enantiomerically pure layers which are symmetry related by a mirror plane and thereby stabilize a non-centrosymmetric structure. This is an attractive approach for the synthesis of non-centrosymmetric crystals, because it does not require enantiopure starting materials. While this strategy does not work in all cases, studies such as this help to better define the conditions under which this strategy can be effective.

## ASSOCIATED CONTENT

**Supporting Information**

X-ray crystallographic data for (*R*)-**1** (CIF)
X-ray crystallographic data for (*S*)-**1** (CIF)
X-ray crystallographic data for (*rac*)-**1** (CIF)
Additional synthetic details, single-crystal X-ray diffraction details, Pawley refinements of PXRD, crystal structure of (*S*)-**1**, CH–π edge-to-face interactions, hydrogen bond lengths and angles, photoluminescence emission data of (*R*)-**1**, magnetic moments and Weiss constants, field-cooled magnetic susceptibility data, PXRD data of (*R*)-**1** after dehydration (DOCX)

**Accession Codes**

CCDC 2348796-2348798 contain the supplementary crystallographic data for this paper; these data can be obtained free of charge via www.ccdc.cam.ac.uk/data_request/cif, or by emailing data_request@ccdc.cam.ac.uk, or by contacting The Cambridge Crystallographic Data Centre, 12 Union Road, Cambridge CB2 1EZ, UK; fax: +44 1223 336033.

## AUTHOR INFORMATION

### Corresponding Author

*E-mail: woodward.55@osu.edu

### ORCID

Joseph T. Race: 0000-0002-8551-3627

Cierra Foster: 0009-0002-0835-915X

Patrick M. Woodward: 0000-0002-3441-2148

### Author Contributions

JTR and PMW prepared the manuscript. JTR performed the synthesis, crystallography, optical measurements, and thermal measurements. CF collected, fit, and analyzed the magnetic data. All authors have given approval to the final version of the manuscript.

### Notes

The authors declare no competing financial interest.

## ACKNOWLEDGMENT

Funding was provided by the National Science Foundation under Award DMR-2003793.

## REFERENCES

(1) Ying, T.-T.; Shi, H.-J.; Chen, S.-P.; Tang, Y.-Z.; Tan, Y.-H.; Wang, S.-F.; Sun, Z.; Wang, F. X.; Wan, M.-Y. Large Spontaneous Polarization Ferroelectric Property, Switchable Second-Harmonic Generation Responses, and Magnetism in an Fe-Based Compound. *Inorg. Chem.* **2023**, *62* (15), 6189–6195.

(2) Vijayakanth, T.; Liptrot, D. J.; Gazit, E.; Boomishankar, R.; Bowen, C. R. Recent Advances in Organic and Organic–Inorganic Hybrid Materials for Piezoelectric Mechanical Energy Harvesting. *Adv. Funct. Mater.* **2022**, *32* (17), 2109492.

(3) Ahn, J.; Ma, S.; Kim, J. Y.; Kyhm, J.; Yang, W.; Lim, J. A.; Kotov, N. A.; Moon, J. Chiral 2D Organic Inorganic Hybrid Perovskite with Circular Dichroism Tunable over Wide Wavelength Range. *J. Am. Chem. Soc.* **2020**, *142* (9), 4206–4212.

(4) Chen, Z.; He, Y.; Zhang, Y.; Zhang, X.-M.; Fu, D. Ultraviolet–Visible-Near-Infrared Photoresponses Realized in a Polar Dion–Jacobson Hybrid Perovskite through Light-Induced Pyroelectric Effects. *Chem. Mater.* **2023**, *35* (19), 8192–8202.

(5) Ok, K. M.; Chi, E. O.; Halasyamani, P. S. Bulk Characterization Methods for Non-Centrosymmetric Materials: Second-Harmonic Generation, Piezoelectricity, Pyroelectricity, and Ferroelectricity. *Chem. Soc. Rev.* **2006**, *35*, 710–717.

(6) Li, X.; Hoffman, J. M.; Kanatzidis, M. G. The 2D Halide Perovskite Rulebook: How the Spacer Influences Everything from the Structure to Optoelectronic Device Efficiency. *Chem. Rev.* **2021**, *121* (4), 2230–2291.

(7) Mao, L.; Chen, J.; Vishnoi, P.; Cheetham, A. K. The Renaissance of Functional Hybrid Transition-Metal Halides. *Acc. Mater. Res.* **2022**, *3* (4), 439–448.

(8) Dang, Y.; Liu, X.; Cao, B.; Tao, X. Chiral Halide Perovskite Crystals for Optoelectronic Applications. *Matter*. **2021**, *4*, 794-820.

(9) Wang, Y.; Nisbet, M. L.; Kamp, K. R.; Hiralal, E.; Gautier, R.; Halasyamani, P. S.; Poeppelmeier, K. R. Beyond π-π Stacking: Understanding Inversion Symmetry Breaking in Crystalline Racemates. *J. Am. Chem. Soc.* **2023**, *145* (30), 16879–16888.

(10) Moon, T. H.; Oh, S. J.; Ok, K. M. [((*R*)-$C_8H_{12}N)_4$][$Bi_2Br_{10}$] and [((*S*)-$C_8H_{12}N)_4$][$Bi_2Br_{10}$]: Chiral Hybrid Bismuth Bromides Templated by Chiral Organic Cations. *ACS Omega* **2018**, *3* (12), 17895–17903.

(11) Billing, D. G.; Lemmerer, A. Synthesis and Crystal Structures of Inorganic-Organic Hybrids Incorporating an Aromatic Amine with a Chiral Functional Group. *CrystEngComm* **2006**, *8* (9), 686–695.

(12) Troyanov, S. I.; Feist, M.; Kemnitz, E. Syntheses and Crystal Structures of Novel Bromoferrates(III), Chloro-, and Aquachloroferrates(III) with Tetrahedral and Octahedral Iron Coordination, among them two Neutral Complexes of Iron(II) and (III). *Z. Anorg. Allg. Chem.* **1999**, *625*, 806–812.

(13) James, B. D.; Skelton, B. W.; White, A. H. The *mer*-Triaquatrichloroiron(III) Molecule in Triethylenediammonium and Piperazinium Chloride Matrices. *Z. Anorg. Allg. Chem.* **2008**, *634* (2), 262–266.

(14) SAINT Version 8. Bruker AXS Inc.: Madison, Wisconsin, USA. 2016.

(15) SADABS Version 2016/2. Bruker AXS Inc.: Madison, Wisconsin, USA. 2016.

(16) Sheldrick, G. M. SHELXT – Integrated Space-Group and Crystal-Structure Determination. *Acta Cryst.* **2015**, *71* (1), 3–8.

(17) Sheldrick, G. M. Crystal Structure Refinement with SHELXL. *Acta Cryst.* **2015**, *71* (1), 3–8.

(18) Coelho, A. A. TOPAS and TOPAS-Academic: An Optimization Program Integrating Computer Algebra and Crystallographic Objects Written in C++. *J. Appl. Cryst.* **2018**, *51* (1), 210–218.

(19) Momma, K.; Izumi, F. VESTA 3 for Three-Dimensional Visualization of Crystal, Volumetric and Morphology Data. *J. Appl. Cryst.* **2011**, *44* (6), 1272–1276.

(20) OriginPro 9.0.0. OriginLab Corporation: Northampton, MA, USA.

(21) Dance, I. G.; Freeman, H. C. The Crystal Structure of Dichlorotetraaquochromium(III) Chloride Dihydrate: Primary and Secondary Metal Ion Hydration. *Inorg. Chem.* **1965**, *4* (11), 1555–1561.

(22) Diaz-Moreno, S.; Munoz-Paez, A.; Martinez, J. M.; Pappalardo, R. R.; Sanchez Marcos, E. EXAFS Investigation of Inner- and Outer-Sphere Chloroaquo Complexes of $Cr^{3+}$ in Aqueous Solutions. *J. Am. Chem. Soc.* **1996**, *118* (50), 12654–12664.

(23) Elving, P. J.; Zemel, B. Absorption in the Ultraviolet and Visible Regions of Chloroaquochromium(III) Ions in Acid Media. *J. Am. Chem. Soc.* **1957**, *79* (6), 1281–1285.

(24) *Absorption Spectra in the Ultraviolet and Visible Region*, 10th ed.; Lang, L., Ed.; Academic Press, 1968.

(25) Woodward, P. M.; Karen, P.; Evans, J. S. O.; Vogt, T. *Solid State Materials Chemistry*; Cambridge University Press: Cambridge, UK, 2021.

(26) Gautier, R.; Klingsporn, J. M.; Van Duyne, R. P.; Poeppelmeier, K. R. Optical Activity from Racemates. *Nat. Mater.* **2016**, *15* (6), 591–592.

(27) Fucaloro, A. F.; Forster, L. S.; Rund, J. V; Lin, S. H. $^2E$ Relaxation in Mixed-Ligand $Cr(NH_3)_{6-n}X_n$ Complexes. *J. Appl. Phys* **1983**, *87*, 1796–1799.

(28) Forster, L. S. The Photophysics of Chromium(III) Complexes. *Chem Rev* **1990**, *90* (2), 331–353.

(29) Mannei, E.; Asedegbega-Nieto, E.; Ayari, F. Thermal Treatment of Anhydrous Chromium (III) Chloride: Thermodynamic Study. *Thermochim Acta* **2022**, *707*, 179102.

(30) Abramchuk, M.; Jaszewski, S.; Metz, K. R.; Osterhoudt, G. B.; Wang, Y.; Burch, K. S.; Tafti, F.; Abramchuk, M.; Jaszewski, S.; Metz, K. R.; Osterhoudt, G. B.; Wang, Y.; Burch, K. S.; Tafti, F. Controlling Magnetic and Optical Properties of the van Der Waals Crystal $CrCl_{3-x}Br_x$ via Mixed Halide Chemistry. *Adv. Mater.* **2018**, *30* (25), 1801325.

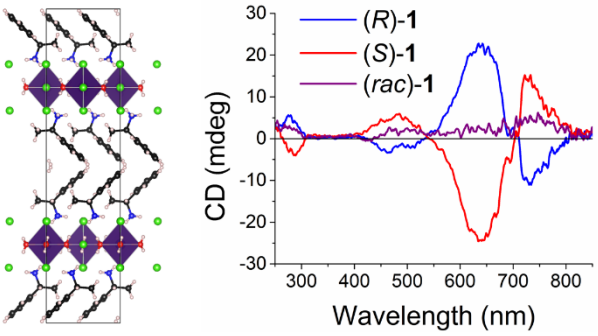


Synopsis: Synthesis, crystal structure solution, optical characterization, magnetic characterization, and thermal stability of three co-crystals between *mer*-$[Cr^{III}Cl_3(H_2O)_3]^0$ and (*R/S*)-α-methylbenzylammonium chloride.